



An experimental investigation of deep dynamic stall control using plasma actuators

David Castañeda¹ · Nicole Whiting² · Nathan Webb³ · Mo Samimy³

Received: 26 April 2021 / Revised: 4 January 2022 / Accepted: 9 March 2022 / Published online: 6 April 2022
© The Author(s), under exclusive licence to Springer-Verlag GmbH Germany, part of Springer Nature 2022

Abstract

The effect of active control by a nanosecond pulsed dielectric-barrier discharge plasma actuator was studied on a NACA 0012 airfoil, with a 7-inch chord (with 13-inch endplates) and a 14-inch span, for a sinusoidal motion profile from $\alpha = 0^\circ$ to 20° at $Re_c = 300,000$ and $k = 0.075$. Characterization of the baseline flow highlighted the dominant influence of the dynamic stall vortex (DSV) and the subsequent separation, during the downstroke, on the aerodynamic forces. PIV results confirmed that actuation over a wide range of frequencies generates structures of various size and spacing through the manipulation of the Kelvin–Helmholtz instability. The results showed that the dominant DSV, present in the baseline case, was replaced by the structures induced by actuation. The effects of control on the flow field were used to explain the changes in aerodynamic loading, providing insight into the underlying physics of the observed control authority. Peak aerodynamic loads (lift, drag, and moment) were all reduced by control. Control also augmented the lift during the downstroke (separated flow), reduced lift hysteresis (responsible for vibratory loading), and increased the cycle-averaged lift-to-drag ratio.

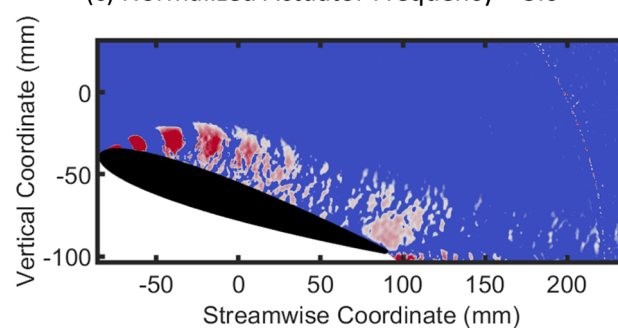
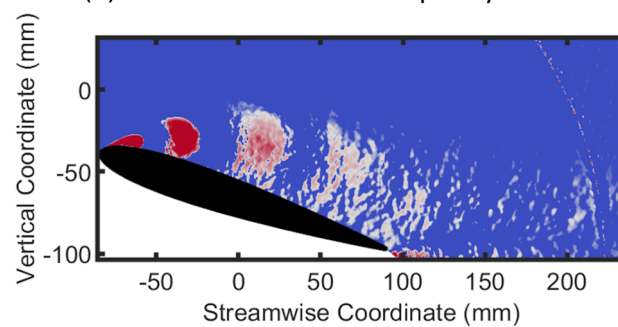
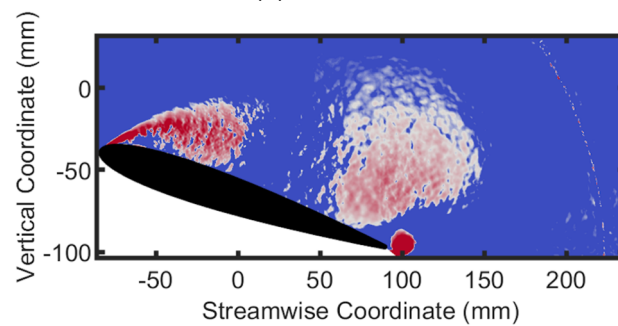
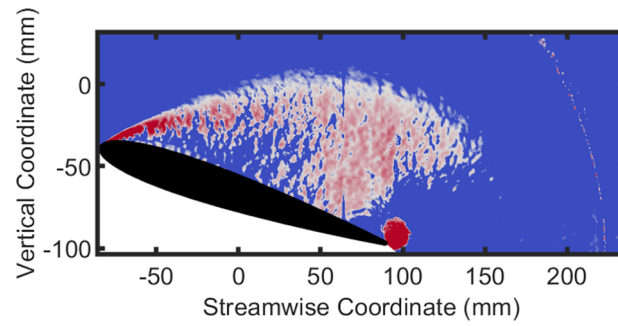
✉ Nathan Webb
webb.356@osu.edu

¹ Universidad del Valle, Cali, Colombia

² Honda Development and Manufacturing of America LLC,
Raymond, OH, USA

³ The Ohio State University, Columbus, OH, USA

Graphical abstract



Phase-Averaged Swirling Strength Maps (Vortex-Identification Method) from Phase-Locked PIV Measurements at an Angle-of-Attack of 19.2° during the Upstroke, for Various Excitation Conditions

List of symbols

b	Airfoil span
c	Airfoil chord
C_L	Sectional lift coefficient $\left(\frac{2L}{\rho u_\infty^2 cb}\right)$
C_M	Sectional moment coefficient $\left(\frac{2M}{\rho u_\infty^2 c^2 b}\right)$
C_D	Sectional drag coefficient $\left(\frac{2D}{\rho u_\infty^2 cb}\right)$
D	Drag force
f_e	Excitation frequency
f_{osc}	Frequency of the airfoil pitch oscillation
h/c	Vertical distance from the pitching axis to the tunnel floor/ceiling (h) normalized by the airfoil chord
k	Airfoil motion reduced frequency $\left(\frac{\pi c f_{osc}}{u_\infty}\right)$
L	Lift force
L/D	Cycle-averaged lift to drag ratio
M	Moment about $x/c = 0.25$
Re_c	Reynolds number based on airfoil chord $\left(\frac{\rho u_\infty c}{\mu}\right)$
St_e	Normalized excitation frequency $\left(\frac{f_e c}{u_\infty}\right)$
u_∞	Freestream velocity
x/c	Chordwise coordinate, origin at the airfoil leading edge, normalized by the airfoil chord
α	Airfoil angle of attack
α_{max}	Maximum (during oscillation) airfoil angle of attack
α_{min}	Minimum (during oscillation) airfoil angle of attack
ΔC_L	Difference between upstroke and downstroke lift coefficient at a given α (lift hysteresis)
μ	Dynamic viscosity
Ξ_{cycle}	Cycle-averaged aerodynamic damping coefficient $\left(-\frac{4}{\pi(\alpha_{max}-\alpha_{min})^2} \oint C_m d\alpha\right)$
ρ	Density

1 Introduction

Dynamic stall is a time-dependent flow separation and stall phenomenon that occurs due to rapid motion of a lifting surface. The dynamic stall phenomenon is present in many applications: maneuvering aircraft, wind turbines, natural flyers, rotorcraft, and others. Due to its unsteady nature, the flow remains attached at angles greater than the typical static stall angle of attack. At the eventual stall onset, the dynamic stall vortex (DSV) develops. This vortex forms at the leading edge and convects along the upper surface of the airfoil, generating a moving low-pressure region. The maximum lift exceeds that typically achievable under steady conditions, and a more negative (nose-down) pitching moment is experienced (McCroskey et al. 1976). Eventually, the DSV reaches the trailing edge and is shed into the wake, leaving

behind a fully separated flow and causing an abrupt loss of lift (McAlister et al. 1978). The enumerated transient forces can have significant negative effects in the various applications in which dynamic stall occurs. In rotorcraft, for example, the large unsteady aerodynamic loads associated with dynamic stall subject the high aspect ratio rotor blades to large torsional loads and excessive vibration, which can cause structural damage. To avoid this, the performance envelope (specifically the forward flight speed) is limited (Leishman 2006).

Dynamic stall is an extremely complex phenomenon with many interacting elements. A particularly influential element is the formation and convection of the DSV, which has been studied by many authors (Carr 1988; Gardner et al. 2013; McAlister et al. 1978; McCroskey et al. 1981). To avoid the adverse effects of dynamic stall, the DSV must be weakened or suppressed. In rotorcraft, the benefits of controlling dynamic stall include the reduction of loads on the blades and the ability to increase the forward flight speed. The common requirements for control methods include robustness of control authority, durability, and ability to withstand high centrifugal forces. Other necessary characteristics include low weight, required power, and cost (Leishman 2006). Methods of active and passive flow control, to mitigate the adverse consequences of dynamic stall, have been widely compiled (Choudhry et al. 2016; Corke and Thomas 2015; Lorber et al. 2000). Some passive flow control technologies for dynamic stall control include vortex generators (Heine et al. 2013), trailing-edge flaps (Gerontakos and Lee 2006), and leading-edge droop (Chandrasekhara et al. 2004). While various passive flow control methods have proven beneficial in specific flight regimes, airfoil shape modifications can increase the weight of the blade and become a source of noise and vibration, resulting in detrimental effects at off-design conditions. While active flow control techniques require additional power, add complexity, and may become inoperable, the flexibility to provide benefit across a wide range of operating conditions motivates research into active flow control solutions. Active flow control actuator technologies include synthetic jets (Traub et al. 2004), pulsating jets (Greenblatt and Wagnanski 1999), and plasma actuators (Post and Corke 2004). Due to their weight, robustness, power use, and resistance/immunity to high centrifugal forces, plasma actuators are an excellent candidate for flow control and mitigation of dynamic stall. Preliminary results documenting the use of plasma actuators injecting momentum into the flow for the control of dynamic stall are promising (Post and Corke 2006). Specifically, the addition of momentum to the flow, for the mitigation of dynamic stall, was investigated and found to be quite effective for low/medium Reynolds number flows. While the results were excellent, momentum-based

flow control struggles to retain control authority in high Reynolds number flows. Nanosecond Pulsed Dielectric-Barrier Discharge (NS-DBD) actuators, on the other hand, produce relatively high-amplitude, high-bandwidth thermal perturbations for effective instability-based flow control (Roupassov et al. 2009). Specifically, they can excite the Kelvin–Helmholtz (K-H) flow instability over a wide range of flow speeds and Reynolds numbers (Samimy et al. 2018). A NS-DBD plasma actuator has been shown to trigger the formation of vortices over an airfoil at a static angle of attack (α) (Samimy et al. 2019). The characteristics of these structures including size, organization, and entrainment capabilities are controlled by the excitation frequency of the perturbations. Recall that the DSV plays a critical role in the dynamic stall process. The control authority of the NS-DBD actuator requires proper leveraging of existing flow physics, as it exploits the K-H instability to manipulate the structure formation. Thus, a proper understanding of dynamic stall flow physics is required to effectively implement this control technique. Additionally, the performance of the excitation may provide insight into the relevant or dominant physics of the phenomenon.

Previous work in dynamic stall flow control, using NS-DBD plasma actuators, has been conducted by Singhal et al. (2018). They examined the control of dynamic stall on a sinusoidally oscillating NACA 0015 airfoil driven by a timing belt oscillating mechanism. Nine combinations of reduced frequency (normalized airfoil oscillation frequency, k) and Reynolds number were tested. The excitation Strouhal numbers (St_e) were of order 1 for low St_e and of order 10 for high St_e . The excitation results were documented using surface pressure measurements (to determine the aerodynamic force coefficients) and PIV images. Three primary trends for deep dynamic stall control were observed: (1) low St_e excitation caused unsteady loads in the stalled stage, (2) excitation led to earlier flow reattachment, and (3) high St_e excitation reduced aerodynamic hysteresis, negative aerodynamic damping, and DSV strength. However, although the results of Singhal et al. (2018) were interesting, they were exploratory and preliminary in nature. Thus, the experiments' quality needed to be improved, and the conclusions confirmed.

The objectives of the current work are: (1) to demonstrate and quantify the effectiveness of a NS-DBD plasma actuator for dynamic stall flow control, and (2) to better understand the dynamic stall physics relevant to this type of flow control. This paper presents the design and validation of an upgraded experimental setup and baseline and excited flow results (PIV and aerodynamic force measurements) for one dynamic stall case. The actuator was demonstrated to produce various beneficial control effects and the excitation conditions necessary for various effects elucidate the relevant physics.

2 Experimental arrangement

This section describes the new, upgraded setup. Further details of the experimental setup used in this work can be found in Castañeda (2020).

2.1 Facility

The experimental setup was installed in the optically clear acrylic test section of the subsonic recirculating wind tunnel at the Gas Dynamics and Turbulence Laboratory, within the Aerospace Research Center at The Ohio State University. The test section has a 61 cm \times 61 cm (2 ft \times 2 ft) cross-section and a 122 cm (4 ft) length. The flow velocities can be varied from 15 to 95 m/s. The clear test section provides optical access for particle image velocimetry (PIV) measurements on various planes.

A NACA 0012 airfoil, with a 7-inch chord and an aspect ratio of 2, was cantilever mounted in a vertical orientation in the test section. The NACA 0012 airfoil profile was selected because it is suitable for rotorcraft applications (Greenblatt and Wagnanski 2003; Leishman 2006), one (of many) application for dynamic stall flow control. Additionally, it has been widely studied in literature at various conditions (Ham 1972; Lee and Gerontakos 2004; McAlister et al. 1978; McCroskey 1987). The airfoil is composed of two pieces, a Polyoxymethylene (Delrin) leading edge on which the NS-DBD actuator is affixed, and a stainless-steel main body. Delrin was chosen for the leading edge due to its material properties and ability to insulate the high-voltage actuator from the metal airfoil. Structural requirements associated with cantilever mounting the airfoil dictated the need for a metal main body. The reason for cantilever mounting the airfoil will be discussed in Sect. 2.2.

The NS-DBD plasma actuator, installed on the airfoil leading edge (Delrin portion), is shown in Fig. 1. It

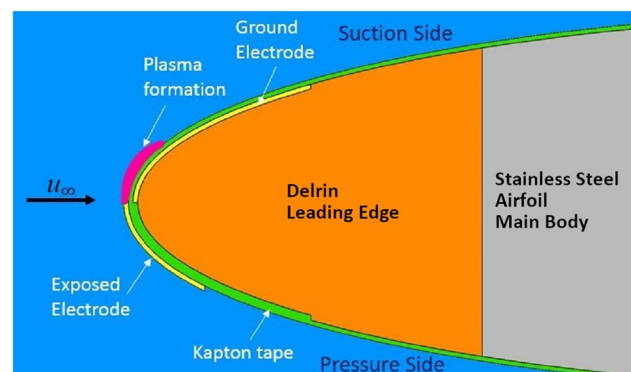


Fig. 1 Cross-sectional view of Delrin leading edge with plasma actuator installed

extended over the entire span of the airfoil and covered from $x/c = 0.024$ on the pressure side to $x/c = 0.055$ on the suction side. The juncture between the plasma actuator's electrodes was located at $x/c = 0$ with the plasma extending onto the suction surface. As discussed at length in previous publications (Clifford et al. 2016; Little et al. 2012; Samimy et al. 2018), the mechanism of this actuation technique is to excite instabilities in the shear layer that exist when the leading-edge flow is separated, specifically, the K-H instability. Not only does this instability respond over a wide range of frequencies, but it also typically manifests in baseline flow at a "preferred mode" range of frequencies, much lower than that of the most-amplified frequency. The preferred mode frequency range typically scales with a flow geometry parameter, in this case, the airfoil chord length. This justifies the use of the airfoil chord length as the length scale used to normalize the excitation frequencies to Strouhal number. Additionally, for nanosecond pulsed actuators, the excitation input manifests as an impulse input, introducing many harmonics which add higher-frequency content to the flow. The underlying physics are quite complex and (as noted above) are explained in detail in Samimy et al. (2018).

The actuator placement (leading edge) was motivated by the receptivity region of the K-H instability, which is the separation line/shear layer origin. For this thin airfoil, which experiences leading-edge stall (note the static-stall curve presented in Sect. 2.3), the separation line will be at or near the leading edge. The actuator is composed of ground and exposed electrodes separated by a dielectric barrier. The self-adhesive copper tape ground electrode is affixed to the Delrin piece and covered with the dielectric layer: three layers of Kapton tape, each 0.09 mm thick, producing a total dielectric strength of 10 kV. Finally, the copper tape exposed electrode is adhered to the airfoil pressure surface (see Fig. 1) completing the plasma actuator. The Delrin leading edge was specially machined with recesses such that the dielectric barrier lies flush with the NACA 0012 profile, and only the exposed copper electrode protrudes. The actuator is pulsed at various frequencies by a high-voltage nanosecond pulse generator, which was custom designed and built at The Ohio State University. A magnetic compression circuit in the pulse generator creates a high voltage and current waveform for the actuator, producing up to a 20 kV pulse with a pulse width from 50 to 100 ns full width at half-maximum (depending on the plasma actuator characteristics). Pulses can be delivered continuously at a rate of up to 3 kHz or higher for a liquid-cooled unit. Details about the pulse generator can be found in Little et al. (2012) and Takashima et al. (2011). These pulse-repetition frequencies are recorded as excitation Strouhal number (St_e) in which the pulsing frequency is normalized by the airfoil chord and the freestream velocity. Recall that the excitation frequency

is (primarily) what determines the size, organization, and entrainment capabilities of the induced structures.

The use of a pulsed actuator results in potential for confusion as both the frequency of airfoil oscillation and the frequency of excitation are highly relevant to this problem. The term "reduced frequency" (k) refers to the normalized frequency of airfoil oscillation. The terms "excitation frequency" and "excitation Strouhal number" (St_e) refer to the frequency at which the actuator is pulsed. Note that phase-averaged measurements (both load cell and PIV) are presented throughout this paper. The measurements are phase-locked/averaged with respect to the airfoil motion frequency, not the excitation frequency. Indeed, the excitation itself is phase-locked to the airfoil motion frequency.

2.2 Upgrades

Despite the promising results obtained with the initial experimental set up (Singhal et al. 2018), its preliminary nature significantly limited the quality of the results in several ways: (1) The setup had a high blockage ratio of up to 18%. (2) The synchronization process between motion and pressure signal was limited to 5 ms. (3) The airfoil motion repeatability was poor: up to 1° cycle-to-cycle variation. To improve the quality of the experiments and verify the results, a new experimental set up was designed, fabricated, and assembled. This system included modifications/upgrades to the airfoil, oscillation driver, and DAQ equipment. The upgraded system is described below.

The airfoil chord and span were reduced, producing a lower blockage ratio. With the reduction in airfoil span, 33 cm (13 inch) diameter endplates were installed to preserve quasi two-dimensional flow. The test airfoil had a chord of 17.8 cm (7 in) and aspect ratio of 2. This reduced the overall blockage to about 10% at $\alpha = 20^\circ$ (including the mount and endplates). Despite this improvement h/c is still relatively low (1.7) (Duraisamy et al. 2007). This resulted in the magnitudes of maximum lift and moment coefficients being larger than the results reported in the literature (Greenblatt & Wygnanski 2001; McCroskey et al. 1982), as expected.

An ATI Industrial Automation Six-Axis Force/Torque Delta 660–60 transducer was used to record the aerodynamic forces and moments. Using this analog transducer (rather than the previously employed ethernet-connected scanning pressure transducers) not only improved the synchronization of the various DAQ and control components (to within 15 μ s), but also significantly increased the temporal resolution of the aerodynamic force measurements. The load cell had a listed uncertainty of less than 0.15% of the maximum measured baseline force and less than 0.08% of the maximum measured baseline moment. This means that the primary source of uncertainty in the measured loads was due

to cycle-to-cycle variation, which was small (see Sect. 2.3 for more details). Use of a load cell required the airfoil to be cantilever mounted (to prevent contamination by reaction forces from a second mount), necessitating the design of the stiffer metal/Delrin airfoil previously described and shown in Fig. 1. Additionally, the orientation was changed to vertical to reduce the load due to the weight of the airfoil (see Fig. 2). The use of a load cell (as opposed to the single-spanwise-location pressure tap array) includes, by default the effect of any potential flow three-dimensionality. This is important, as Esfahani et al. (2018) found that (as expected) three-dimensional effects occurring in the post-stall regime are not captured in aerodynamic forces derived from single-spanwise-location pressure tap arrays. Dell'Orso and Amitay (2018) also observed stall cells under very similar conditions. Esfahani et al. (2018) also found that excitation by a NS-DBD actuator (as employed in this work) can cause three-dimensional effects to develop on a statically stalled airfoil where the baseline flow exhibited primarily two-dimensional characteristics. The load-cell measurements naturally include the contribution of flow three-dimensionality which would not have been captured if a static pressure tap array had been employed. Additionally, it enables the accurate measurement of drag, which can be difficult to obtain using a pressure tap array. Conversely, it also includes wall effects and does not capture chordwise pressure profiles, which can help to elucidate the stall physics/causes. Load-cell measurements were chosen for all the stated advantages over a single-array of pressure taps along the chord. The center of the transducer was aligned with the center of rotation (see Fig. 2). This was chosen to be the quarter-chord axis of the airfoil in accordance with common literature practice (Lee and Gerontakos 2004; McCroskey et al. 1976, 1981; Mulleners and Raffel 2012; Piziali 1994; Singhal 2017).

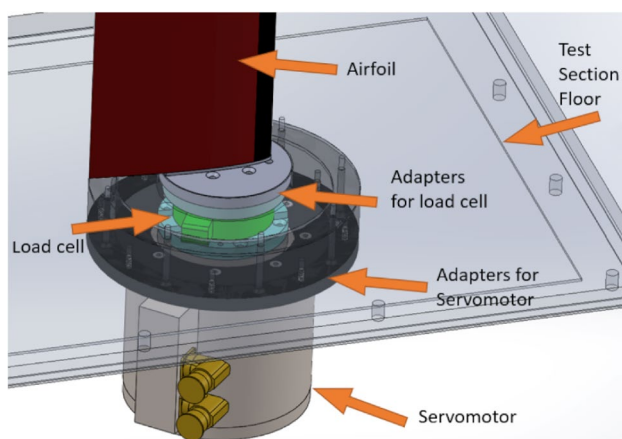


Fig. 2 Diagram of the test section, airfoil, load cell, and motion driving system

As the load cell measures actual forces (not pressures), and the airfoil motion is not steady, inertial forces from the experimental setup contaminate the raw load-cell data. Furthermore, the cantilever mounting of the airfoil results in a relatively low system natural frequency, which can contaminate the measured aerodynamic forces. To eliminate this contamination, the measured forces were processed using the procedure outlined here. First, both wind-on, and wind-off forces were collected. This allows the inertial forces to be eliminated from the raw load-cell data. Two filters were used to remove the system natural frequencies: a band-stop and a low-pass filter. The band-stop filter eliminated the natural frequency of the system while the low-pass filter (a third order Chebyshev type II filter) removed high-frequency noise. Based on literature, the first 2 harmonics of the airfoil motion were retained (to maintain an accurate record of the time-varying forces throughout the oscillation) (Yeo et al. 2012). Both filter transfer functions are passed through a zero-phase digital filter (ensuring zero-phase distortion) and applied to the inertial and total force data before they are subtracted from one another. To determine the natural frequency of the setup (and therefore the frequencies that ought to be filtered out) two techniques were utilized. The first was a hammer impact test. In this method, a hammer impulsively impacts the airfoil, simulating an infinitely short duration impulse. This results in a constant amplitude disturbance being generated across all frequencies. The response of the impulse disturbance is amplified by the structural resonances which can then be identified in spectra of the measured forces. A no-wind test in which the airfoil was oscillated provided a second set of results to corroborate the system natural frequencies discovered by the hammer impact test. The combined results of these methods allowed the appropriate parameters to be selected for the two filters employed. Further details on the filtering process can be found in Whiting (2019) and Castañeda (2020). The aerodynamic loads presented throughout the rest of this paper were extracted via the following procedure: Both the wind-off and wind-on results (collected over a minimum of 50 cycles) were filtered (as described above) to remove the effect of the system natural frequencies. The results were then phase averaged and the wind-off results subtracted from the wind-on. This procedure provided a record of the phase-averaged aerodynamic forces. The uncertainty introduced by the filtering procedure is difficult to quantify, but stems from variations in the natural frequencies being filtered. These frequencies are governed by the mass of the experimental arrangement, as well as its mechanical properties. As these are presumed constant throughout the experimental campaign, the uncertainty introduced by the filtration procedure may safely be neglected. Figure 3 shows the effects of the filtration procedure on the raw baseline normal force component. Note that both curves include the effect of inertial

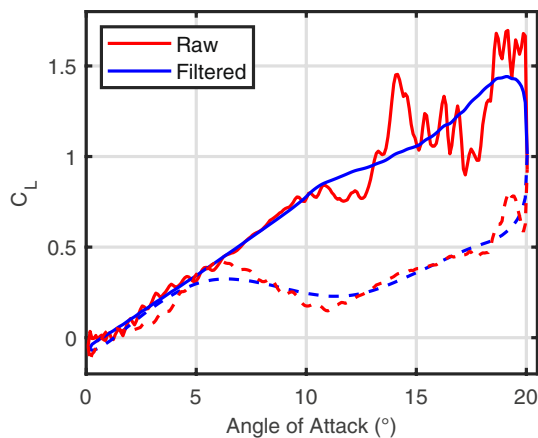


Fig. 3 Comparison of raw and filtered phase-averaged load cell results

forces, which is not eliminated by the filter, but by subtraction of the wind-off results.

A Kollmorgen Housed Direct Drive Rotary (DDR) servomotor DH063M-13 with an AKD servo drive was selected for the motion system. By using a direct-drive servo, with the load cell (and airfoil) directly mounted to it, uncertainties associated with the timing belt gearing and slop were eliminated from the power transmission system, allowing excellent motion repeatability to be obtained. The selected servo can deliver a peak torque of 160 N-m and a maximum rotational velocity of 500 rpm.

The data acquisition/servo control system was a NI-cRIO model 9035, which was selected for its real-time processing, user programmable FPGA, and interchangeable modules for a variety of instrumentation. The NI-cRIO also natively supports the AKD servo drive and communicates with it via EtherCAT, while NI Softmotion provides the motion control required to establish a repeatable airfoil motion profile. The load data and airfoil position were acquired simultaneously, along with two pressure transducers which monitor the wind-tunnel flow state. The simultaneous acquisition of the force measurement and airfoil motion systems by the FPGA provided synchronization better than 15 μ s.

In addition to the load cell and tunnel monitoring pressure measurements, a commercially available LaVision PIV system was used to measure two velocity components in a streamwise/vertical plane at the tunnel centerline (see Fig. 4). Two cameras were employed to increase the field-of-view. Images were captured with a time-delay of 25 μ s. To obtain velocity fields which were phase-locked to the airfoil motion, images were acquired at a multiple of the motion frequency, acquiring 6 images (at different α) throughout one motion cycle. External triggering from the servo encoder was used to ensure the image acquisition remained synchronized with the airfoil motion. For each baseline

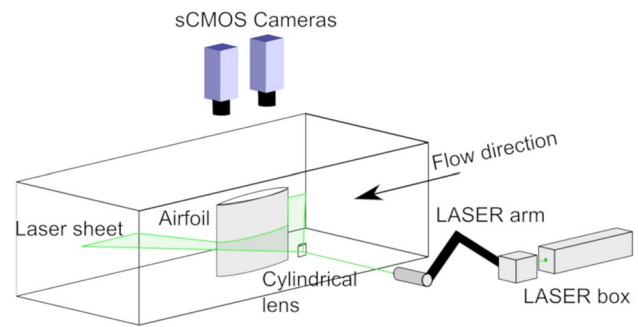


Fig. 4 Schematic of 2-component PIV arrangement: cameras, optics, and laser sheet in relation to the airfoil

and excitation phase, 500 images pairs were collected. The images were processed using DaVis 8.3. After application of a time filter and masking, a sequential, multi-pass cross-correlation algorithm, with a final pass of a 24×24 -pixel interrogation window with 75% overlap, was employed to generate the vector fields. To reduce the spurious vectors, post-processing operations were employed between passes. After processing, the two vector fields from the cameras were merged. Calculation of the statistics and vortex swirling strength was performed in DaVis.

2.3 Apparatus validation

The most foundational aspect of the upgraded experimental setup is its ability to provide an accurate, repeatable motion, which is crucial to obtain accurate cycle-averaged results. The observed maximum cycle-to-cycle variation over 126 cycles of a sinusoidal motion profile from $\alpha = 8^\circ$ to 18° is less than 0.01° . This motion is highly repeatable and confirms that the physical arrangement itself is suitable for the study of dynamic stall flow control.

To further validate the apparatus, the measured aerodynamic loads were also examined. The baseline flow over the NACA 0012 airfoil was documented for several different combinations of chord-based Reynolds number ($Re_c = 300,000, 500,000, 700,000$) and reduced frequency ($k = 0.025, 0.05, 0.075$). Only results for $Re_c = 300,000$ and $k = 0.075$ will be presented in this paper. The remainder of these results are presented in Castañeda (2020). The servo-driven airfoil motion system makes the adoption of various motion profiles relatively easy. The focus of this paper is on the effects of active flow control in the context of a deep dynamic-stall event, and therefore the motion profile examined in this paper is nearly sinusoidal (there is a slight kink due to the motor controller in the motion profile during the upstroke), with a minimum and maximum α of 0° and 20° respectively. This is well above the approximately 14° static stall angle of attack of the NACA 0012 airfoil at $Re_c = 300,000$, as shown in Figs. 5, 6, 7.

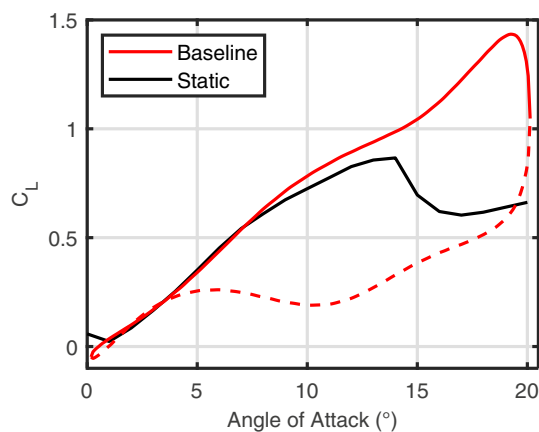


Fig. 5 Sectional lift coefficient vs. angle of attack (α) for baseline (uncontrolled) flow. Solid and dashed lines show upstroke and downstroke motions, respectively

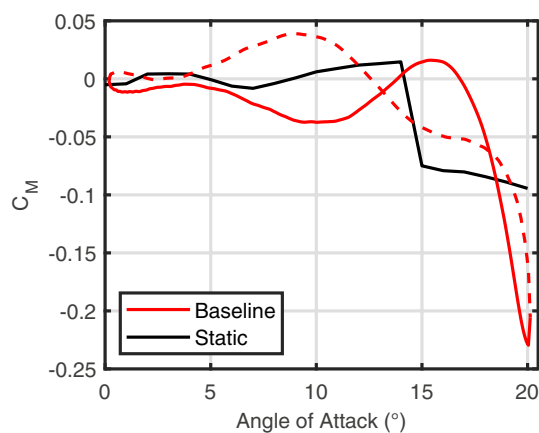


Fig. 6 Sectional moment coefficient vs. angle of attack (α) for baseline (uncontrolled) flow. Solid and dashed lines show upstroke and downstroke motions, respectively

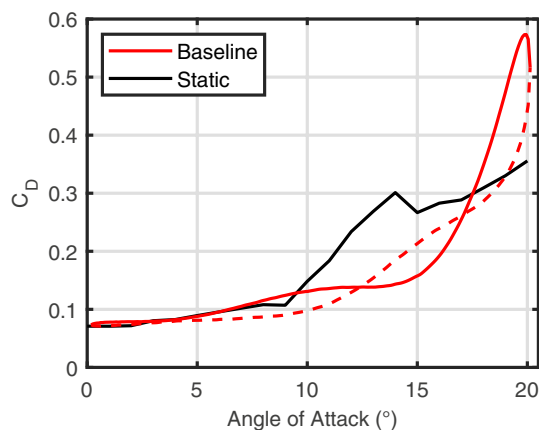


Fig. 7 Sectional drag coefficient vs. angle of attack (α) for baseline (uncontrolled) flow. Solid and dashed lines show upstroke and downstroke motions, respectively

Figures 5, 6, 7 show the processed (filtered, phase-averaged, inertial forces removed) aerodynamic force data. The key features of deep dynamic stall are clearly visible (for instance, the peak in all 3 aerodynamic forces due to the convection of the DSV) further validating the experimental setup. It should also be noted that, when examining the raw, unfiltered, non-phase averaged load cell results, no significant cycle-to-cycle variation, including bifurcation, was observed (Castañeda 2020). Quantitatively, for the baseline case, the maximum variation in cycle-to-cycle raw normal force at a single point was less than 8% of the maximum measured normal force. The maximum cycle-to-cycle variation averaged over one cycle was less than 4%. Though it is best to avoid presenting phase-averaged results for a stochastic process such as dynamic stall, the investigation of the raw results confirmed that the phase-averaged results presented here are representative of the flow. Experiments reported in the literature have observed a bifurcation in the measured aerodynamic forces from dynamic stall over a pitching airfoil (Harms et al. 2018; Ramasamy et al. 2016). It is interesting to note that this bifurcation was observed in aerodynamic force data obtained by integrating static pressure measurements collected from one array of static pressure transducers (i.e., no spanwise resolution). There is potential for three-dimensionality in these flows ((Smith et al. 2020)), especially the controlled flows (Esfahani et al. 2018). The lack of bifurcation observed in the current (load-cell collected, i.e., all three-dimensional effects included) results suggests that three-dimensional effects may indeed be present in dynamic stall under certain flow/motion conditions. This suggests that a variety of measurement techniques will be required to completely understand the effects of control on dynamic stall, especially considering the extremely high aspect ratio airfoils typically associated with dynamic stall applications. It may also encourage caution when examining apparent discrepancies between data collected with different measurement techniques.

3 Results

3.1 Baseline flow field

It is imperative to obtain detailed information about the dominant flow dynamics, as it is these physical phenomena which guide the flow control application. Phase-locked PIV results of the baseline flow provide a tool to accomplish this. Of particular interest are the formation and convection of the DSV and the presence/absence and extent of separation over the airfoil. Thus, both swirling strength maps (a vortex identification technique to track the DSV and other flow structures, see (Adrian et al. 2000) for a details) and streamwise-velocity fields (for the location and extent of

separation) of the baseline flow are presented and discussed prior to examining the controlled cases.

Maps of phase-averaged, normalized swirling strength, calculated on a streamwise plane along the spanwise center of the airfoil, from 2-component PIV results, are presented in Fig. 8. The blue tint indicates values from 0 to 0.2 and the red tint indicates values from 0.2 to 1. The formation and convection of the DSV are highlighted by the swirling strength, a vortex identification method. The DSV is a phenomenon of critical importance to the dynamic stall process as it causes the primary detrimental effects associated with dynamic stall (specifically strong, transient aerodynamic loads and decreased aerodynamic damping, i.e., the potential for aerodynamic flutter). In the first image ($\alpha = 14.50^\circ \uparrow$) the flow is unremarkable. The load-cell results displayed in Fig. 5 show this to be within the linear regime, while the effects of the DSV were not observed until higher angles of attack (a conclusion corroborated by these PIV results). In contrast, at $\alpha = 17.84^\circ \uparrow$, the DSV is clearly visible, located at approximately $x/c = 0.75$. The DSV (and associated low-pressure region) covers a significant part of the airfoil suction surface. This corresponds to the observed lift coefficient increase (see Fig. 5). Secondly, notice that at $\alpha = 16.44^\circ \uparrow$ the

DSV (and the associated low-pressure region) is upstream of $x/c = 0.25$ (the pitching axis of the airfoil), while at the higher angles of attack, it has moved downstream. This corresponds perfectly to the observed positive (nose-up) and negative (nose-down) moment excursions (see Fig. 6) associated with moment stall. The direction of the closed loops in the moment coefficient (clockwise (CW) or counter-clockwise (CCW)) determines their contribution (negative or positive respectively) to the aerodynamic damping coefficient. Thus, the timing of the DSV relative to the motion emerges as a parameter of critical importance. Recall that the NS-DBD actuator specifically seeds the flow with perturbations to control the timing and organization of structures (of which the DSV is one).

The separation of the flow over the suction surface of the airfoil also has a significant effect on the aerodynamic forces. Figure 9 displays phase-averaged streamwise velocity fields at a variety of α 's. The use of a 2-tone colormap (red and blue, with white representing zero velocity) allows easy identification of regions of separation. Note that while the exact definition of separation is the point at which the in-plane velocity (relative to the dynamically pitching airfoil suction surface) goes to zero, the definition implicitly

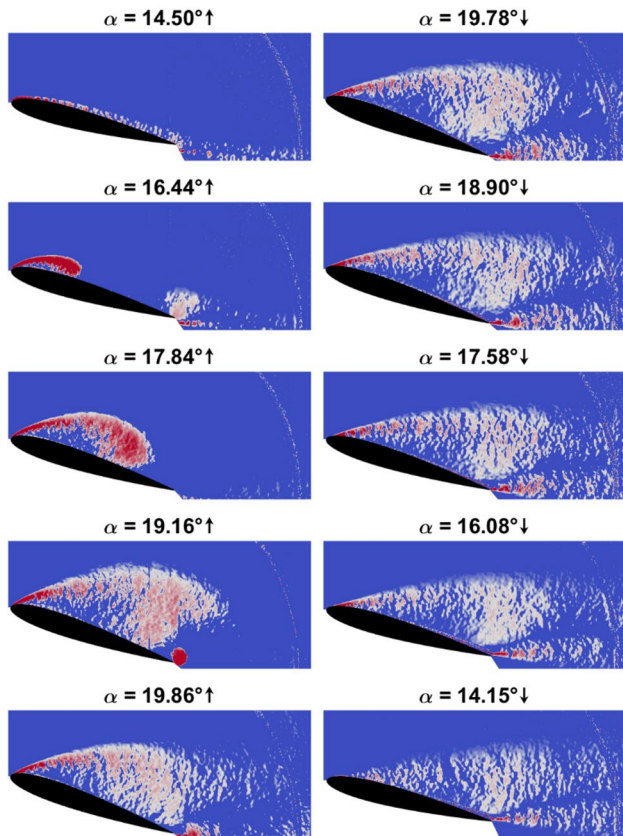


Fig. 8 Baseline phase-averaged swirling strength maps from phase-locked PIV measurements

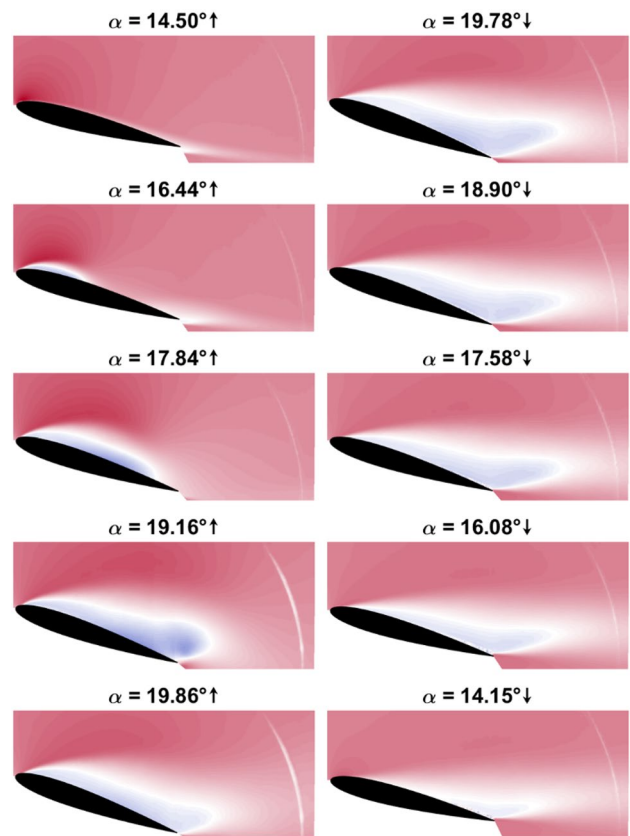


Fig. 9 Baseline phase-averaged streamwise velocity maps from phase-locked PIV measurements (white is zero streamwise velocity)

employed by Fig. 9 (and subsequent similar figures) is that the separation boundary is where the streamwise velocity (in the tunnel reference frame) is zero. This is a good surrogate for the true separation region and a consistent metric for the comparison of the baseline and controlled results. At $\alpha = 14.50^\circ \uparrow$ the flow is not separated, as expected and inferred from the load-cell results. Comparing Fig. 8 with Fig. 9 shows that the leading-edge separation region propagates downstream with the DSV. The downstream side of the DSV introduces downwash which will aid flow attachment, while the upstream side introduces upwash which encourages flow separation. Once the DSV has passed downstream of the airfoil, the drag slowly decreases (see Fig. 7). The reason for the slow rate of decrease is likely the presence of the massive separation which follows the DSV. This again demonstrates the extreme importance of the DSV and the timing of its formation and convection. These processes are observed to have a dominant effect on aerodynamic loading through the effect of the associated low-pressure region and the effect on the development of the separation region.

3.2 Controlled flow field

As discussed above, the aerodynamics strongly depend on the timing and convection of the DSV. As described previously, the NS-DBD actuator employed in this work exerts control authority by leveraging natural instabilities to control structure formation in the flow. Thus, they are employed in the current work to target the formation, convection, and timing of the DSV. As described in Sect. 2.1, one NS-DBD actuator was installed at the airfoil leading edge to provide perturbations to the flow over the suction side of the airfoil. The primary variable excitation parameter was the frequency (i.e., timing of the DSV) at which the perturbations were introduced. The effects of the NS-DBD actuator on the dynamic stall flow field are examined in this section. Section 3.3 will relate these observed flow field alterations to the appropriate aerodynamic load effects. This analysis will elucidate why different types of excitation produce the effects they do.

Figures 10, 11, 12 show swirling strength maps, calculated from PIV results, for various excitation conditions. The excited flow fields clearly show that the excitation is modifying the organization and size of the structures as they form and convect downstream over the airfoil. Specifically, the distance between adjacent structures correlates with the period of the excitation frequency, as expected. Thus, the excitation frequency controls the timing, organization, and size of the structures that form over the airfoil. This also provides clear evidence that the control mechanism is not boundary layer tripping (despite the lower Reynolds number). For example, Fig. 11 at $\alpha = 17.75^\circ \uparrow$ shows that many coherent structures have been generated by excitation

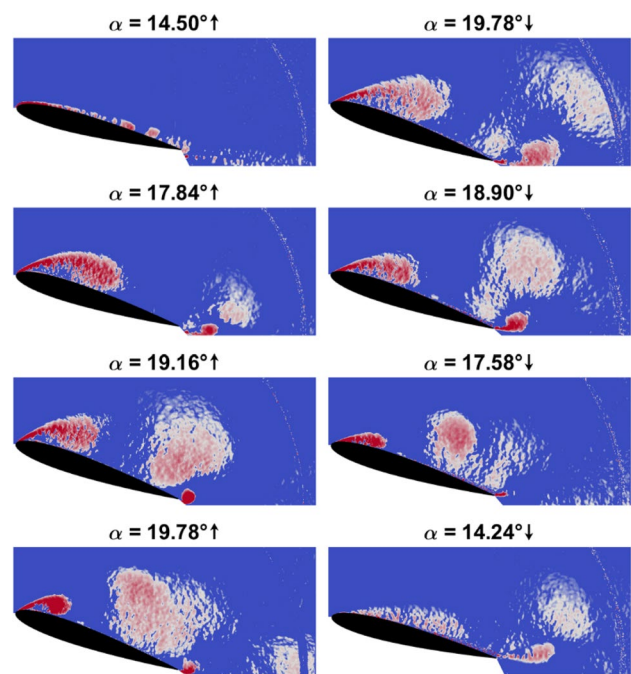


Fig. 10 Phase-averaged swirling strength maps from phase-locked PIV measurements for $St_e = 0.5$

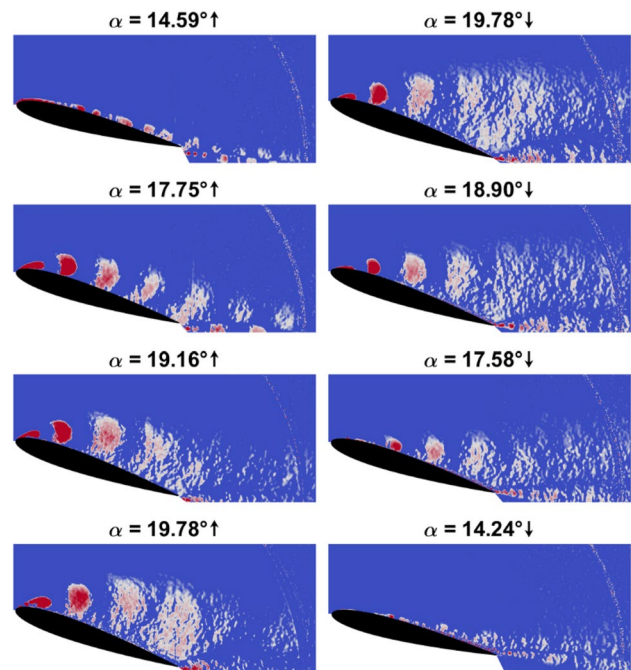


Fig. 11 Phase-averaged swirling strength maps from phase-locked PIV measurements for $St_e = 3.0$

prior to stall. This is not the result of tripping which results in a turbulent boundary layer with randomly distributed structures in the flow. Rather, this is a clear production of

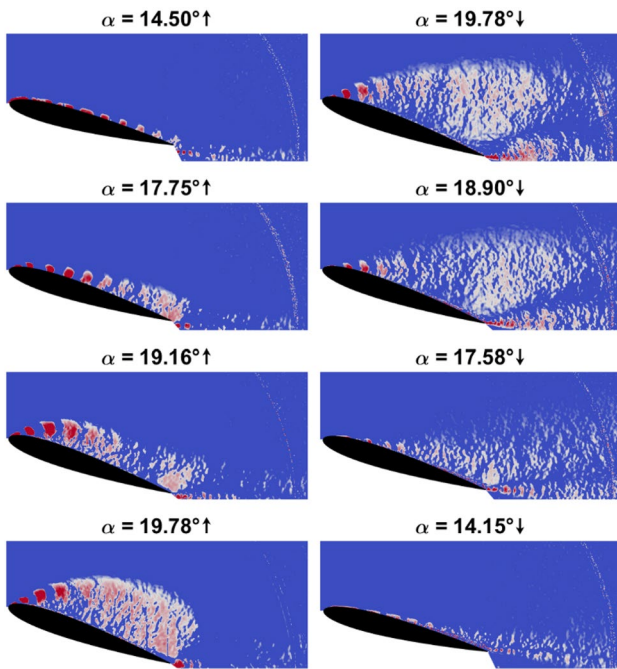


Fig. 12 Phase-averaged swirling strength maps from phase-locked PIV measurements for $St_e=8.0$

large-scale coherent structures which convect along the airfoil, with the separation distance correlated with the excitation frequency. In higher frequency excited cases ($St_e=3.0$ and 8.0), there is no sign of the large, dominant DSV present in the baseline case: The structures generated by the excitation have replaced the DSV. The working hypothesis is that, by triggering periodic structure formation, control prevents vorticity from building up at the leading edge. Continuously bleeding vorticity from the leading edge does not allow the DSV to form. Instead, it is replaced by structures of character determined by the excitation frequency. As stated above, the effects of excitation on the aerodynamic forces are explored in Sect. 3.3 and the observed effects of control explained in light of these PIV results.

The details of the resulting structures provide insight into optimal excitation conditions for various desired results. First, larger structures are more coherent and persist a greater streamwise distance. Second, they have more ability to entrain high-momentum freestream flow (i.e., they will be able to more fully suppress the separation). The second point will be revisited when examining the streamwise velocity maps below and confirmed by the load-cell results in Sect. 3.3. The results shown in Figs. 10, 11, 12 are consistent with the first. In the $St_e=0.5$ case, the large structures retain strong coherence well beyond the trailing edge of the airfoil. In contrast, in the $St_e=3$ case, the medium-sized structures appear to retain coherence to about $x/c=0.75$ and the small structures in the $St_e=8$ case become indistinguishable at

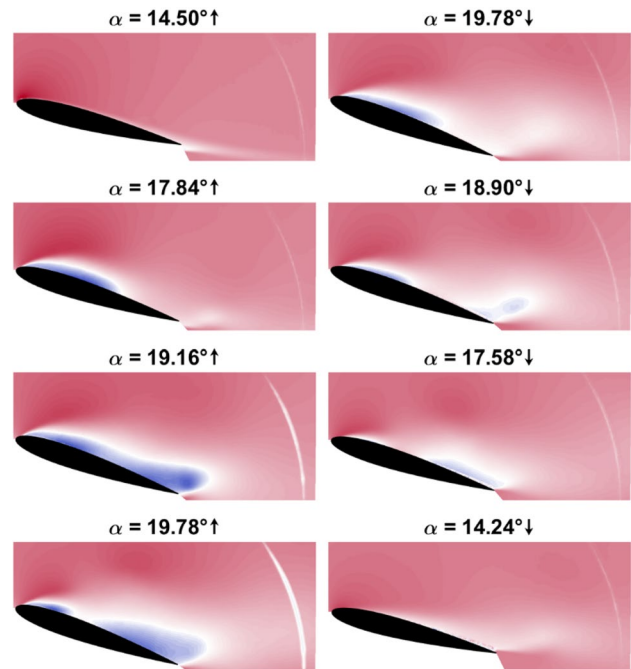


Fig. 13 Phase-averaged streamwise velocity maps from phase-locked PIV measurements for $St_e=0.5$ (white is zero streamwise velocity)

around $x/c=0.5$. It is possible that phase averaging could cause such an apparent effect; however, results presented below suggest that the smaller structures are indeed dissipating more quickly. It is also important to note that, while the larger structures produced in the lower frequency excitation cases are likely more persistent and entrain more fluid, they may produce more unsteady effects, due to their shedding from the trailing edge and the larger spacing between them. Conversely, the smaller-scale structures produce more constant effects, as they have a smaller spacing between them and (likely) disintegrate before the trailing edge.

Figures 13, 14, 15 show phase-locked streamwise velocity fields at various excitation conditions corresponding to the cases shown in Figs. 10, 11, 12. These figures can be used to evaluate the stated hypothesis, that larger structures (produced by lower frequency excitation) will more effectively mitigate the separation. This can be observed during the downstroke. The $St_e=0.5$ case shows (at about $x/c=0.75$ for $\alpha=18.90^\circ\downarrow$) the highest speed flow on the suction surface of all the excitation conditions (c.f. Figures 14, 15 for $\alpha=18.90^\circ\downarrow$). This observation is further supported by the load cell results presented in Sect. 3.3. The separation control is observed to be intermittent though, as suggested above, with the separation at about $x/c=0.25$ being significantly worse than in the higher-frequency excitation cases. Indeed, the separated and attached regions track well with the structures observed in Fig. 10. However, as the excitation frequency increases, the flow over the airfoil surface slows,

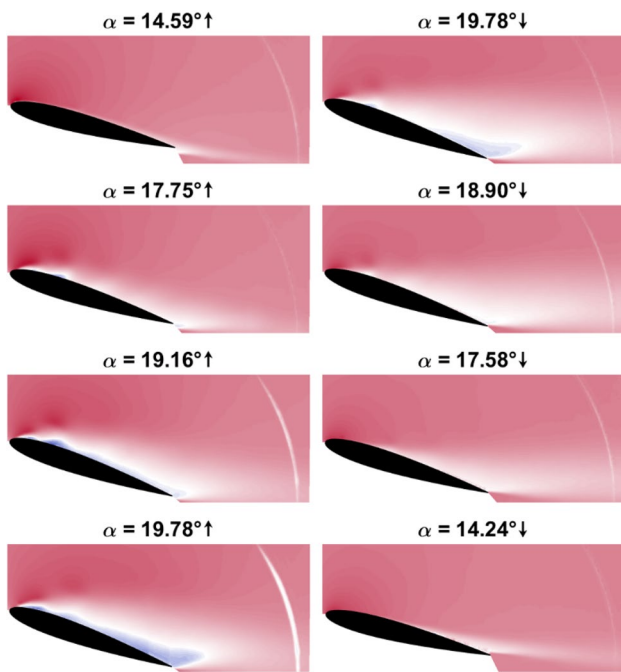


Fig. 14 Phase-averaged streamwise velocity maps from phase-locked PIV measurements for $St_e=3.0$ (white is zero streamwise velocity)

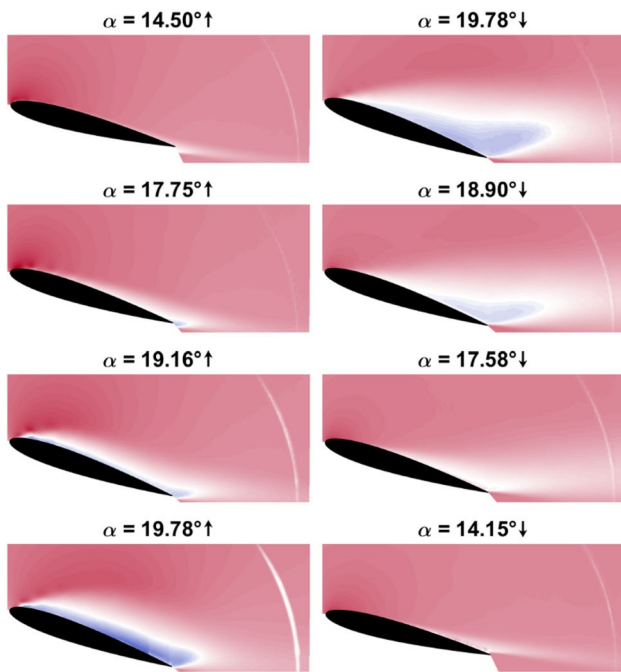


Fig. 15 Phase-averaged streamwise velocity maps from phase-locked PIV measurements for $St_e=8.0$ (white is zero streamwise velocity)

and eventually re-separates near the trailing edge during the downstroke (c.f. Figures 13, 14, 15 for $\alpha = 19.78^\circ \downarrow$). This is consistent with the replacement of the DSV with numerous

small, relatively low-coherence structures which were previously hypothesized to quickly dissipate (see Figs. 11, 12). The region of the airfoil which experiences trailing edge separation increases with increasing excitation frequency (see Figs. 13, 14, 15). This observation is consistent with the hypothesis that the structures are dissipating more rapidly in higher excitation frequency cases.

The upstroke shows a similar trend to the downstroke, but, there are some differences. The most notable of these is that, while the intermittent character of the flow acceleration due to the lowest frequency excitation is apparent, both the higher frequency excitation cases appear to produce greater acceleration of the flow over the airfoil. This is a reversal of the trend observed during the downstroke. While this likely does not affect the overall trend in aerodynamic forces, as the separation and its effects are much more pronounced during the downstroke (see Fig. 5), it is still an interesting observation. Given the presence of the discussed complicating factors, the load-cell results (discussed below) will provide final confirmation of the larger structures greater ability to suppress the separation.

3.3 Controlled aerodynamic loads

The flow field results showcase the important physical phenomena, and the effects of actuation on them. A good understanding of these physics is crucial to understanding how the dynamic stall process will be altered by control. However, from an application standpoint, the effects of control on the aerodynamic loads are paramount.

Figure 16 shows the effect of excitation at different frequencies on the lift coefficient. Control effects are observed during both the upstroke and downstroke. During the upstroke, the peak lift is diminished by excitation. $St_e = 3$ to 8 generated the largest reduction in peak lift. This aligns

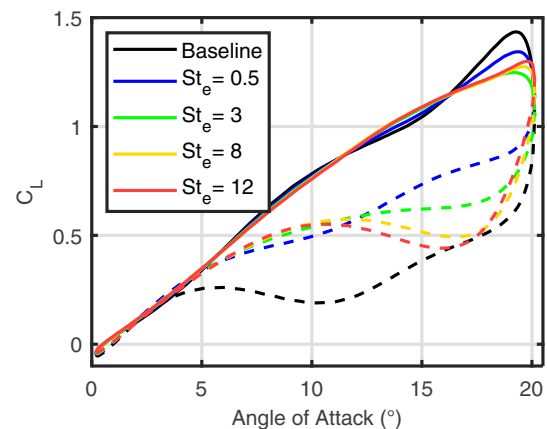


Fig. 16 Sectional lift coefficient vs. angle of attack for various excitation conditions. Solid and dashed lines show upstroke and downstroke motions respectively

with the working hypothesis of the control mechanism and is supported by the PIV results. Recall that the DSV produces significant lift augmentation. The higher frequency excitation cases replace the DSV with smaller, less-coherent structures (c.f. Figures 8, 11, 12). This reduces the effect of the structures' associated low-pressure regions, decreasing the overall lift augmentation. Figure 16 suggests that if excitation frequency is too high, the structures become so small and dissipate so quickly that they begin to lose their effectiveness (inferred from the increased peak lift at high St_e). However, even in this case there is some effect, as the DSV-associated lift peak is delayed to a higher angle of attack. It is possible that another control mechanism is in play here. Visbal and Benton (2018) observed such a delay of the DSV by ultra-high-frequency excitation ($St_e = 12.5$ was their lowest tested frequency). They attributed this to the control manipulation of natural instabilities in the laminar separation bubble at the airfoil leading edge.

During the downstroke, structures generated by the actuation reattach the flow, augmenting the lift. Low excitation Strouhal numbers are more effective for this augmentation than high excitation Strouhal numbers. The trend is quite clear: increasing excitation frequency results in reduced cycle-averaged lift during the downstroke. This trend is consistent with the presence of large-scale, coherent structures formed by lower frequency excitation (see Fig. 10) and confirms the previously stated hypothesis that larger structures more effectively mitigate the separation.

The data is reduced for further analysis using maximum lift hysteresis: the largest difference between the upstroke and downstroke lift coefficient. Figure 17 plots this value against excitation frequency, with the baseline case shown as $St_e = 0$. This metric describes the degree of load variation (relevant for structural vibration assessment) experienced by the airfoil. This is because much of the hysteresis

is caused by the DSV convection and the separation formation. Thus, the maximum hysteresis often describes the magnitude of the rapid lift change near the maximum α . In the best case, the lift hysteresis is reduced by up to 45%. The optimal excitation frequency (for lift hysteresis reduction) is $St_e = 0.5$. As discussed above, this excitation condition produces large-scale structures with significant entrainment capabilities. Recall that under these conditions the peak lift is only somewhat reduced, while the low-lift region, due to separation, is significantly augmented (see Fig. 16). Thus, while the strong, transient nature of the DSV certainly contributes to the lift hysteresis, the separation has a much larger effect. The upward trend in maximum lift hysteresis bears this out: as previously observed in the PIV results (see Figs. 10, 11, 12), increasing the excitation frequency results in progressively smaller structures (with lower entrainment capabilities). This deep dynamic stall case has a large separation region (see Fig. 9) suggesting that significant entrainment capabilities are required to maintain flow attachment. The difference in optimal excitation conditions for various components of this flow (e.g., peak lift vs. lift hysteresis) highlights the complexity of this flow field. Additionally, the differing requirements of various applications must be understood to effectively implement optimal control.

Excitation also has a significant effect on the aerodynamic moment experienced by the airfoil. In particular, Fig. 18 clearly shows that at all tested frequencies, excitation reduces the peak negative (pitch-down) moment experienced by the airfoil, reducing both the magnitude of the unsteady loading, as well as the potential for aerodynamic flutter. The trend in peak moment is similar to that observed in peak lift. Specifically, that increasing excitation frequency to $St_e = 3$ reduces the peak moment magnitude. Further increasing excitation frequency results in decreased excitation effectiveness and delayed peak moment (similar to the trend observed

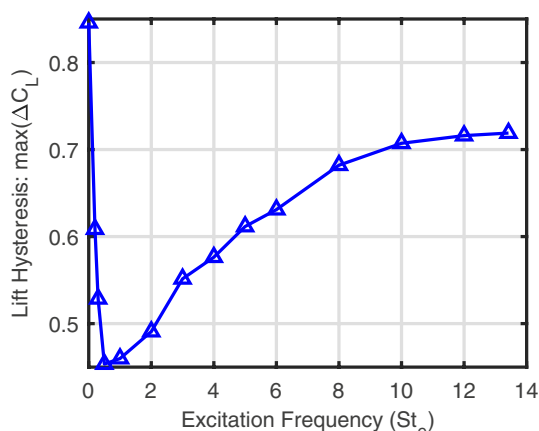


Fig. 17 Lift hysteresis (maximum difference between upstroke and downstroke lift coefficient) vs. excitation frequency

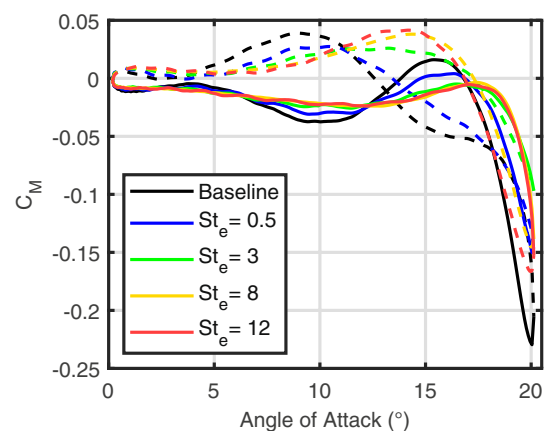


Fig. 18 Sectional moment coefficient vs. angle of attack for various excitation conditions. Solid and dashed lines show upstroke and downstroke motions respectively

in the lift coefficient). This supports the postulate that the DSV evolution is the dominant factor in determining both the lift and moment peaks.

The previously observed decreased excitation effectiveness at very high frequencies (see Fig. 16) also results in increased peak moment (see Fig. 18). As observed in Figs. 10, 11, 12, lower frequency excitation results in larger, more coherent structures convecting over the airfoil. These structures produce an increase in the downstroke lift by mitigating the separation (Figs. 13, 14, 15), allowing the flow to reattach sooner. Here, the effect of the lower frequency excitation structures is to reduce the moment, due to the low-pressure regions associated with the vortices downstream of $x/c = 0.25$. As excitation frequency increases, the vortices become less coherent and dissipate more quickly. The observed trend in aerodynamic moment aligns with both observations. Further support of this trend can be found in the effect of excitation on the downstroke separation extent (see Figs. 13, 14, 15).

Another major effect of pitching moment is its potential to cause aerodynamic flutter. The moment can excited flutter when, in a cycle-integrated sense, is in-phase with the pitching motion, potentially causing the pitching motion to grow without bound (especially on a high-aspect ratio rotorcraft blade) resulting in aerodynamic flutter and extreme structural stress. The relative timing of the DSV shedding and convection in the deep dynamic stall regime (i.e., during the upstroke) makes flutter much less likely to occur than in the light dynamic stall regime. However, it is still an important parameter to examine. Figure 19 shows the cycle-averaged aerodynamic damping coefficient as a function of excitation frequency. This quantity was calculated by integrating the phase-averaged aerodynamic moment coefficient (see the nomenclature section for the exact definition). While the damping coefficient is positive at all tested excitation

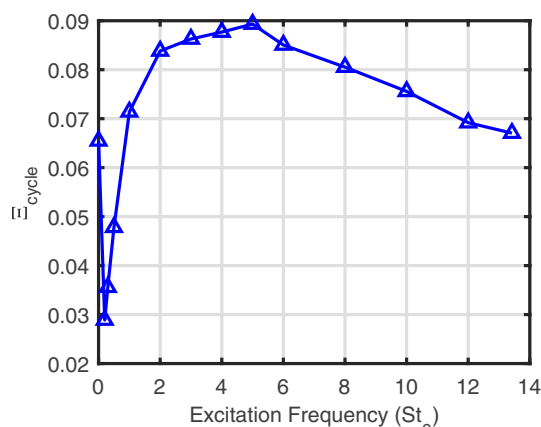


Fig. 19 Cycle-averaged aerodynamic damping vs. excitation frequency

frequencies (i.e., there is no possibility for aerodynamic flutter to occur), it is interesting to note that, for the extremely low excitation frequencies (i.e., those which do a better job reattaching the separation during the downstroke) the damping coefficient is actually decreased relative to the baseline (a detrimental effect). Referral to Figs. 10, 11, 12 makes the reason for this clear. The low-frequency excitation generates multiple, large scale, highly coherent structures during the downstroke. The associated low-pressure regions produce a pitch-down moment (adding to/in-phase-with the pitch down motion) similar to the baseline. This can be observed in Fig. 18 from about 20° to 14° during the downstroke. Additionally, the reduction (relative to the baseline) in peak aerodynamic moment (i.e., pitch-down moment during the upstroke) nearly eliminates the positive contribution to aerodynamic damping found in the baseline. As excitation frequency increases, however, the aerodynamic damping coefficient rapidly increases, surpassing the baseline and leveling off at around $St_e = 5$. Again, this beneficial effect is explained by referencing the PIV results and Fig. 18. By generating many, small, lower-coherence structures, the higher frequency excitation not only decreases the pitch-down moment experienced during the downstroke, but also suppresses/delays the DSV. This reduces the pitch-up moment experienced during the upstroke. Both effects decrease negative contributions to the aerodynamic damping, resulting in an overall increase (beneficial effect).

Finally, as expected, due to the clearly observed effect of excitation on the DSV (c.f. Figure 8 and Figs. 10, 11, 12) the trend in peak drag reduction is similar to that observed for the peak lift and peak moment (see Fig. 20). This makes sense as the DSV exerts a transverse force on the airfoil. As the airfoil is at a non-zero α when the DSV sheds, reduction in transverse force (by excitation) results in reduced drag, as well as lift. Furthermore, the effect of excitation on DSV timing (as noted in the discussion associated with Fig. 16) can also be observed here. Specifically, the rise in drag (associated with the transverse force of the DSV) occurs at a much lower angle (during the upstroke) for the $St_e = 0.5$ case than for the $St_e = 12$ case. As with the other aerodynamic loads, the reduction in (transient) peak drag is beneficial and desirable, though in rotorcraft applications it may be washed out by the cyclic variation in Reynolds number. Though cyclic drag may not have as significant an effect on the rotor blade structural requirement as the lift or moment, an unsteady drag puts a cyclic loading on the engine and drive components and is therefore worth reducing.

As the trends in lift and drag are so similar, it is reasonable to ask if the excitation is merely imitating a Reynolds-number reduction. To address this query, cycle-averaged lift-to-drag ratio is plotted in Fig. 21 for a variety of excitation conditions. These results clearly show that the aerodynamic efficiency (L/D) is significantly increased

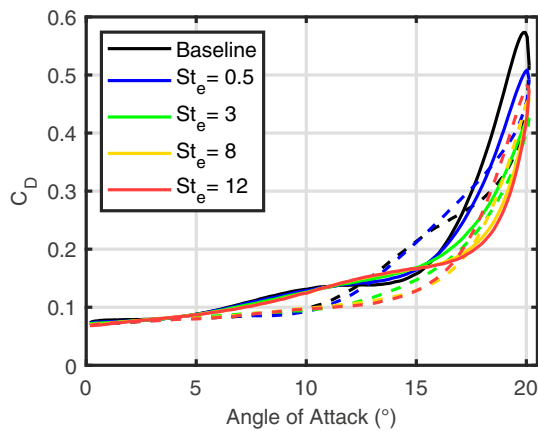


Fig. 20 Sectional drag coefficient vs. angle of attack for various excitation conditions. Solid and dashed lines show upstroke and downstroke motions respectively

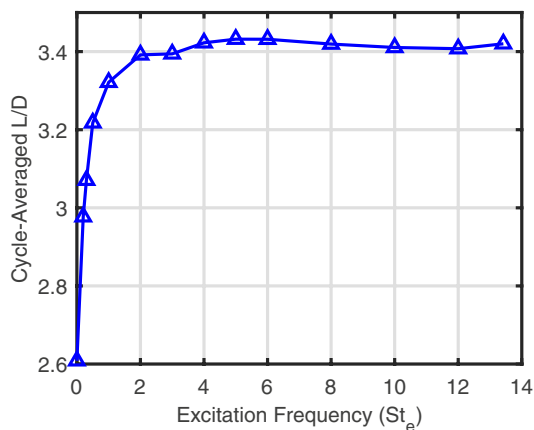


Fig. 21 Cycle-averaged lift-to-drag ratio vs. excitation frequency

by the excitation, up to 30% (with respect to the baseline). Recall that the actuators introduce perturbations of small amplitude (i.e., very small energy inputs). Including the effect of the deposited energy in this measure of aerodynamic efficiency makes negligible difference (less than 0.02% change in the values for the case with the greatest power). Additionally, while both the peak lift and drag reduction (and therefore the structural benefits) begin to decrease as excitation frequency is increased, the airfoil efficiency quickly plateaus and remains relatively constant for $St_e = 2$ and higher. As with any flow control technology, slowly varying effects over a wide range of the design space allows the system response to be more predictable and consistent, easing closed-loop control requirements.

4 Conclusions

The effectiveness of a nanosecond dielectric-barrier discharge (NS-DBD) plasma actuator, for dynamic stall flow control in a deep dynamic stall condition, has been presented in detail, and the dynamic stall physics relevant to this type of flow control have been investigated. Using the newly developed experimental setup, the effect of control by a NS-DBD plasma actuator for a nearly sinusoidal motion profile from $\alpha = 0^\circ$ to 20° at $Re_c = 300,000$ and $k = 0.075$ was studied. First, the experimental setup was validated, and the baseline flow characterized using load cell and PIV results. The dominant influence of the dynamic stall vortex (DSV) and the separation on the aerodynamic forces was shown.

Next, particle image velocimetry (PIV) results of excited flow cases at 3 different frequencies confirmed that the NS-DBD actuator generates structures of various size and spacing through the manipulation of the Kelvin–Helmholtz instability. These structures were observed to vary, depending upon excitation frequency, both in their entrainment capabilities (as deduced from the streamwise velocity and load cell results) and apparent streamwise persistence (i.e., the chordwise point at which they begin to disintegrate, and their effect to evaporate). Furthermore, the phase-locked PIV measurements clearly showed that the dominant DSV present in the baseline case is replaced by the structures induced by excitation. The influence of these excitation-induced structures on the DSV and separation provides a basis to understand the observed effects of control on the aerodynamic loads.

Load cell results show the peak aerodynamic loads (lift, drag, and moment) are all reduced by control. As excitation frequency increased (i.e., smaller structures were produced) the peak loads decreased. However, at a certain point, the structures became too small (likely dissipating too quickly), resulting in higher peak loads. The optimal excitation frequency for peak load reduction is around $St_e = 3$. The control also has a beneficial effect on the aerodynamic loading during the downstroke, particularly on the lift. In this case, it is the lower frequency excitation ($St_e = 0.5$), with its large structures of high-entrainment capabilities, that is most effective at mitigating the separation. This produces the observed augmentation in downstroke lift.

Finally, the effect of excitation on a few airfoil performance metrics was also examined. Specifically, the lift hysteresis (responsible for vibratory loading) is reduced by up to 45%. Due to the natural timing and convection of the DSV, during this deep dynamic stall case, excitation at low frequencies has a detrimental effect on cycle-averaged aerodynamic damping. However, the effect is small enough

that there is no potential for aerodynamic flutter to occur. The cycle-averaged lift-to-drag ratio is increased by up to 30% (at $St_e = 5$ to 6).

The observed trends in aerodynamic lift, drag, and moment all reflect the understanding of the dominant physics revealed by the PIV results. As the DSV has a dominant effect on the flow, using the actuation to replace the DSV with structures of various spacing, coherence, and entrainment capabilities has, as expected, a significant effect on the aerodynamic forces. This highlights the importance of developing a good understand of the underlying physics of the flow and flow control, allowing for intelligent optimization of the implemented control. This is especially important considering the difference in optimal excitation conditions for various components of this flow (e.g., peak lift vs. lift hysteresis). Additionally, the differing requirements of various applications must be understood to effectively implement optimal control. For example, in a wind turbine application, aerodynamic efficiency might be paramount, while for a rotorcraft application, increased aerodynamic damping is critical. The understanding of the underlying physics developed here can aid in the selection of appropriate excitation conditions for given applications. Overall, the NS-DBD was demonstrated to produce a variety of effects over a wide range of potentially desirable flow adjustments.

Acknowledgements The Fulbright-MinCiencias fellowship from Colombia, supporting David Castañeda, and the NASA/Ohio Space Grant Consortium fellowship, supporting Nicole Whiting, are greatly appreciated. Partial support from the Air Force Research Laboratory (with Dr. Miguel Visbal) is gratefully acknowledged.

References

- Adrian R, Christensen K, Liu Z-C (2000) Analysis and interpretation of instantaneous turbulent velocity fields. *Exp Fluids* 29:275–290
- Carr L (1988) Progress in analysis and prediction of dynamic stall. *J Aircr* 25(1):6–17. <https://doi.org/10.2514/3.45534>
- Castañeda D (2020) Active Control of Flow over an Oscillating NACA0012 Airfoil [Dissertation]. The Ohio State University
- Chandrasekhara M, Tung C, Martin P (2004) Aerodynamic Flow Control using a Variable Droop Leading Edge Airfoil (Technical Report RTO-MP-AVT-111). NATO.
- Choudhry A, Arjomandi M, Kelso R (2016) Methods to control dynamic stall for wind turbine applications. *Renew Energy* 86:26–37. <https://doi.org/10.1016/j.renene.2015.07.097>
- Clifford C, Singhal A, Samimy M (2016) Flow control over an airfoil in fully reversed condition using plasma actuators. *AIAA J* 1:1–9. <https://doi.org/10.2514/1.J054157>
- Corke T, Thomas F (2015) Dynamic stall in pitching airfoils: aerodynamic damping and compressibility effects. *Annu Rev Fluid Mech* 47:479–505. <https://doi.org/10.1146/annurev-fluid-010814-013632>
- Dell’Orso H, Amitay M (2018) Parametric investigation of stall cell formation on a NACA 0015 airfoil. *AIAA J* 56(8):3216–3228. <https://doi.org/10.2514/1.J056850>
- Duraisamy K, McCroskey W, Baeder J (2007) Analysis of wind tunnel wall interference effects on subsonic unsteady airfoil flows. *J Aircr* 44(5):1683–1690. <https://doi.org/10.2514/1.28143>
- Esfahani A, Webb N, Samimy M (2018) Stall cell formation over a post-stall airfoil: effects of active perturbations using plasma actuators. *Exp Fluids* 59(132):1–16. <https://doi.org/10.1007/s00348-018-2588-y>
- Gardner A, Richter K, Mai H, Altmikus A, Klein A, Rohardt C-H (2013) Experimental investigation of dynamic stall performance for the EDI-M109 and EDI-M112 airfoils. *J Am Helicopter Soc* 58(1):1–13
- Gerontakos P, Lee T (2006) dynamic stall flow control via a trailing-edge flap. *AIAA J* 44(3):469–480. <https://doi.org/10.2514/1.17263>
- Greenblatt D, Wagnanski I (1999) Parameters affecting dynamic stall control by oscillatory excitation. <https://doi.org/10.2514/6.1999-3121>
- Greenblatt D, Wagnanski I (2001) dynamic stall control by periodic excitation, part 1: NACA 0015 parametric study. *J Aircr* 38(3):430–438. <https://doi.org/10.2514/2.2810>
- Greenblatt D, Wagnanski I (2003) Effect of leading-edge curvature on airfoil separation control. *J Aircr* 40(3):473–481. <https://doi.org/10.2514/2.3142>
- Ham N (1972) Some recent MIT research on dynamic stall. *J Aircr* 9(5):378–379. <https://doi.org/10.2514/3.58995>
- Harms T, Nikooueyan P, Naughton J (2018) Experimental Evaluation of the Cycle-to-Cycle Variation of Dynamic Stall on the SC1094R8 Airfoil. 2018–1267, 1–15. <https://doi.org/10.2514/6.2018-1267>
- Heine B, Mulleners K, Joubert G, Raffel M (2013) Dynamics stall control by passive disturbance generators. *AIAA J* 9:1–12. <https://doi.org/10.2514/1.J051525>
- Lee T, Gerontakos P (2004) Investigation of flow over an oscillating airfoil. *J Fluid Mech* 512:313–341
- Leishman J (2006) Dynamic stall. Principles of helicopter aerodynamics. Cambridge University Press, pp 525–566
- Little J, Takashima K, Nishihara M, Adamovich I, Samimy M (2012) Separation control with nanosecond-pulse-driven dielectric barrier discharge plasma actuators. *AIAA J* 50(2):350–365. <https://doi.org/10.2514/1.J051114>
- Lorber P, McCormick D, Anderson T, Wake B, MacMartin D, Pollack M, Corke T, Breuer K (2000) Rotorcraft Retreating Blade Stall Control. 2000–2475. <https://doi.org/10.2514/6.2000-2475>
- McAlister K, Carr L, McCroskey W (1978) Dynamic Stall Experiments on the NACA 0012 Airfoil (NASA Technical Paper No. 1100; pp. 1–170)
- McCroskey W (1987) A Critical Assessment of Wind Tunnel Results for the NACA 0012 Airfoil (Technical Memorandum No. 100019). NASA
- McCroskey W, Carr L, McAlister K (1976) Dynamic stall experiments on oscillating airfoils. *AIAA J* 14(1):57–63. <https://doi.org/10.2514/3.61332>
- McCroskey W, McAlister K, Carr L, Pucci S, Lambert O, Indergrand R (1981) Dynamic stall on advanced airfoil sections. *J Am Helicopter Soc* 26(3):40–50
- McCroskey W, McAlister K, Carr L, Pucci S (1982) An experimental study of dynamic stall on advanced airfoil sections. Volume 1: summary of the experiment. (Technical Memorandum No. 84245-VOL1). NASA.
- Mulleners K, Raffel M (2012) The onset of dynamic stall revisited. *Exp Fluids* 52:779–793. <https://doi.org/10.1007/s00348-011-1118-y>
- Piziali R (1994) 2-D and 3-D Oscillating Wing Aerodynamics for a Range of Angles of Attack Including Stall (NASA Technical Memorandum No. 4632; p. 570)
- Post M, Corke T (2004) separation control on high angle of attack airfoil using plasma actuators. *AIAA J* 11:2177–2184. <https://doi.org/10.2514/1.2929>

- Post M, Corke T (2006) Separation control using plasma actuators: dynamic stall vortex control on oscillating airfoils. *AIAA J* 44(12):3125–3135. <https://doi.org/10.2514/1.22716>
- Ramasamy M, Wilson J, McCroskey W, Martin P (2016) Measured Characteristics of Cycle-to-Cycle Variations in Dynamic Stall. 1–34
- Roupassov D, Nikipelov A, Nudnova M, Starikovskii A (2009) Flow separation control by plasma actuator with nanosecond pulsed-periodic discharge. *AIAA J* 47(1):168–185. <https://doi.org/10.2514/1.38113>
- Samimy M, Webb N, Crawley M (2018) Excitation of free shear-layer instabilities for high-speed flow control. *AIAA J* 56(5):1770–1791. <https://doi.org/10.2514/1.J056610>
- Samimy M, Webb N, Esfahani A (2019) Reinventing the wheel: excitation of flow instabilities for active flow control using plasma actuators. *J Phys D Appl Phys* 52(354002):1–16. <https://doi.org/10.1088/1361-6463/ab272d>
- Singhal A, Castañeda D, Webb N, Samimy M (2018) Control of dynamic stall over a NACA 0015 airfoil using NS-DBD plasma actuators. *AIAA J* 56(1):78–89. <https://doi.org/10.2514/1.J056071>
- Singhal A (2017) Unsteady Flow Separation Control over a NACA 0015 using NS-DBD Plasma Actuators [Master's Thesis]. The Ohio State University
- Smith M, Jones A, Ayancik F, Mulleners K, Naughton J (2020) An Assessment of the State of the Art from the 2019 ARO Dynamic Stall Workshop. 2020–2697, 1–21. <https://doi.org/10.2514/6.2020-2697>
- Takashima K, Zuzeek Y, Lempert W, Adamovich I (2011) Characterization of a surface dielectric barrier discharge plasma sustained by repetitive nanosecond pulses. *Plasma Sour Sci Technol* 20(055009):1–11. <https://doi.org/10.1088/0963-0252/20/5/055009>
- Traub L, Miller A, Rediniotis O (2004) Effects of active and passive flow control on dynamic-stall vortex formation. *J Aircr* 41(2):405–408. <https://doi.org/10.2514/1.2591>
- Visbal M, Benton S (2018) Exploration of high-frequency control of dynamic stall using large-eddy simulations. *AIAA J* 56(8):2974–2991. <https://doi.org/10.2514/1.J056720>
- Whiting N (2019) Design and Validation of a New Experimental Setup for Dynamic Stall and Preliminary Control Results [Master's Thesis]. The Ohio State University.
- Yeo D, Atkins E, Bernal L, Shyy W (2012) Experimental Investigation of the Pressure, Force, and Torque Characteristics of a Rigid Flapping Wing. 2012–0849. <https://doi.org/10.2514/6.2012-849>

Publisher's Note Springer Nature remains neutral with regard to jurisdictional claims in published maps and institutional affiliations.